ADVANCED SUSTAINABLE SYSTEMS
www.advsustainsys.com

# Processing Agricultural Cornstalks toward High-Efficient Stable Bifunctional ORR/OER Electrocatalysts

*Yinghui Li, Yuanju Qu, Chaocheng Liu, Jiedong Cui, Ke Xu, Yang Li, Haoyu Shen, Zhouguang Lu, Hui Pan, Tao Xu, and Detao Liu**

**Bifunctional oxygen reduction/oxidation reaction (ORR/OER) electrocatalysts derived from biomass are one of the most valuable materials in terms of sustainability, ecological economy and industrial manufacturing, and are emerging as a desired alternative to the commercial Pt/C and $IrO_2$ catalysts. This work demonstrates the processing of agricultural cornstalk waste of cornstalks into stable bifunctional ORR/OER catalysts with high-performance by a simple and cost-effective strategy. Rich hydrophilic active groups (e.g., hydroxyl groups) in the hierarchical porous structures of the native cornstalks enable the sufficient facile combination with transition metals (e.g., Co, Fe, Zn) and heteroatoms (e.g., B, N) from soluble $Co(NO_3)_2$, $ZnCl_2$, $H_3BO_3$, $NH_4Cl$ in a hydrothermal reaction. The pyrolytic evaporation of $Zn^{2+}$ in a high-temperature carbonization process facilitates the generation of abundant micropores and mesopores to increase specific surface areas (941.44 $m^2\ g^{-1}$) and also hinders aggregation between neighboring transition metals. The synergistic effects of N, B, Fe and Co doping in hierarchical porous biochar-structures contributes to outstanding bifunctional ORR/OER activities and working stabilities, outperforming commercial Pt/C and $IrO_2$ catalysts. Computational results further verify the valuable synergistic contributions based on density-functional theory (DFT). This approach opens up a new possibility for the fabrication of bifunctional biochar-based ORR/OER catalysts from artificial engineering and green processing for sustainable agricultural wastes.**

## 1. Introduction

Rechargeable metal–air batteries and fuel cells have attracted worldwide attentions with clean and renewable energy harvesting owing to their high theoretical specific energy (1086 Wh $kg^{-1}$), low production costs, and environmental friendliness.[1–2] Generally, Oxygen Evolution Reaction (OER) and Oxygen Reduction Reaction (ORR) are two crucial reactions for cathode materials, playing a significant role in emerging electrochemical energy technologies.[3–4] Nowadays, noble metals of such Pt-based matrix are reported to be the most efficient commercial ORR/HER catalysts while Ir/Ru-based matrix is the ideal commercial OER electrocatalysts, due to their outstanding electrocatalytic activities and working stabilities.[5–6] However, the main drawbacks of them including high costs, raw material scarcity, and poor stability restrict their large-scale productions,[7–8] making it utmost urgency to exploring other potential alternatives.

Synergetic contributions from the hybrid carbonous (etc., graphene,[9] carbon nanotubes (CNTs),[10] and polypyrrole[11]) electrocatalysts had been demonstrated as the most promising strategy,[12–13] due to its satisfactory electron conduction, good catalytic activities, and also the exposed active sites.[14–16] For example, porous rGO-$Co_{5.47}N$ electrocatalysts[17] was demonstrated with high half-wave potential and excellent cycling stabilities; and B, N-doped carbon nanotube is used to disperse atomically Co sites to significantly improve ORR properties[18] Zou et al.[19] reported the 2D Fe/Co and N/B Co-doped mesoporous carbon nanosheets (FeCo/NB-Cs) that were synthesized to strategically boost kinetics of oxygen reduction/evolution reaction (ORR/OER). Although the resulting ORR or/and OER electrocatalyst activities are satisfactory, there is still under debate on their practical applications due to the disadvantages of

Y. Li, C. Liu, J. Cui, K. Xu, Y. Li, H. Shen, D. Liu
School of Light Industry and Engineering
South China University of Technology
Guangzhou 510640, P. R. China
E-mail: dtliu@scut.edu.cn

Y. Qu, H. Pan
Joint Key Laboratory of the Ministry of Education
Institute of Applied Physics and Materials Engineering
University of Macau
Macao SAR 999078, P. R. China

The ORCID identification number(s) for the author(s) of this article can be found under https://doi.org/10.1002/adsu.202100343.

DOI: 10.1002/adsu.202100343

Z. Lu
Department of Materials Science and Engineering
Shenzhen Key Laboratory of Interfacial Science
and Engineering of Materials
Guangdong-Hong Kong-Macao Joint Laboratory for Photonic-Thermal-Electrical Energy Materials and Devices
Southern University of Science and Technology of China
Shenzhen 518055, P. R. China

T. Xu
Guangdong Provincial Key Laboratory of Building
Energy Efficiency and Application Technologies
Academy of Building Energy Efficiency
School of Civil, Engineering
Guangzhou University
Guangzhou 510006, P. R. China

high-costs, unsustainability, and the complicated fabrication processes with pollutants releases.

One of the most promising routes is effectively exploring the biobased carbonous precursors from renewable wood or agricultural wastes.[20–21] It is convinced that these bioresources have natural superiorities of rich active groups within hierarchical porous structures, possessing high carbon contents and low costs.[22] Efforts to explore the fabrication of biochar precursors from porphyra,[23] agaric,[24] chitosan,[25–26] cornstalk cores[27] and wood[28] have been recently made in past years. For example, Zhou et al. reported that nitrogen-doped $Fe_3Se_4$/FeSe/partially graphitized carbon ($Fe_3Se_4$/FeSe/NPGC) composites as non-precious-metal air-cathode (ORR) catalysts are obtained using waste biomass (cornstalk cores) as raw material.[27] Zhang et al.[28] processed the wood into N-doped hierarchically porous carbonous precursors (N/HPC) which exhibited perfect ORR performances, however, the investigations of OER activities are not reported. Wang et al.[29] fabricated N-doped biochar precursors using a walnut kernel, but it cannot be used as bifunctional electrocatalysts due to their poor OER activities.[30] Hence, the improved strategies are required when we aim to design well-dispersed and hierarchical porous architectures with high surface areas to maximize catalytically active sites for the biochar-based ORR/OER catalysts.

As we can know, ORR and OER require distinctly different conditions of such electric potential that limits the choose of materials capable of bifunctionally catalyzing both reactions.[31–32] Many studies have previously demonstrated that doping single/dual transition metals (e.g., Fe, Ni, Co, and Cu) or/and heteroatom (e.g., N, S, B, and P) significantly enhanced the electron transport property and ORR/OER catalytic activity of carbonous electrocatalysts.[31–33,27,34–35] In this work, we reported a simple two-step strategy of initial hydrothermal reactions and subsequent carbonization process to process agricultural cornstalks toward stable high-performance bifunctional ORR/OER electrocatalysts doped with Co, Fe, B, N, which derived from the initial treatment with soluble inexpensive $Co(NO_3)_2$, $ZnCl_2$, $H_3BO_3$, $NH_4Cl$ in hydrothermal reaction. The synergistic effects resulted from highly dispersed transition metals and heteroatoms in hierarchical porous biochar-structures contribute high-performance bifunctional ORR/OER activities.

## 2. Results and Discussion

### 2.1. Structural and Morphological Characterizations

As a typical agricultural waste, cornstalks are processed from annual agricultural corn harvestings, and have similar biological porous structures and characteristics compared to those of straws and bamboo, but not the wood (**Figure 1**a–c). It has comparative C element (around 50.19 wt%) and O element (around

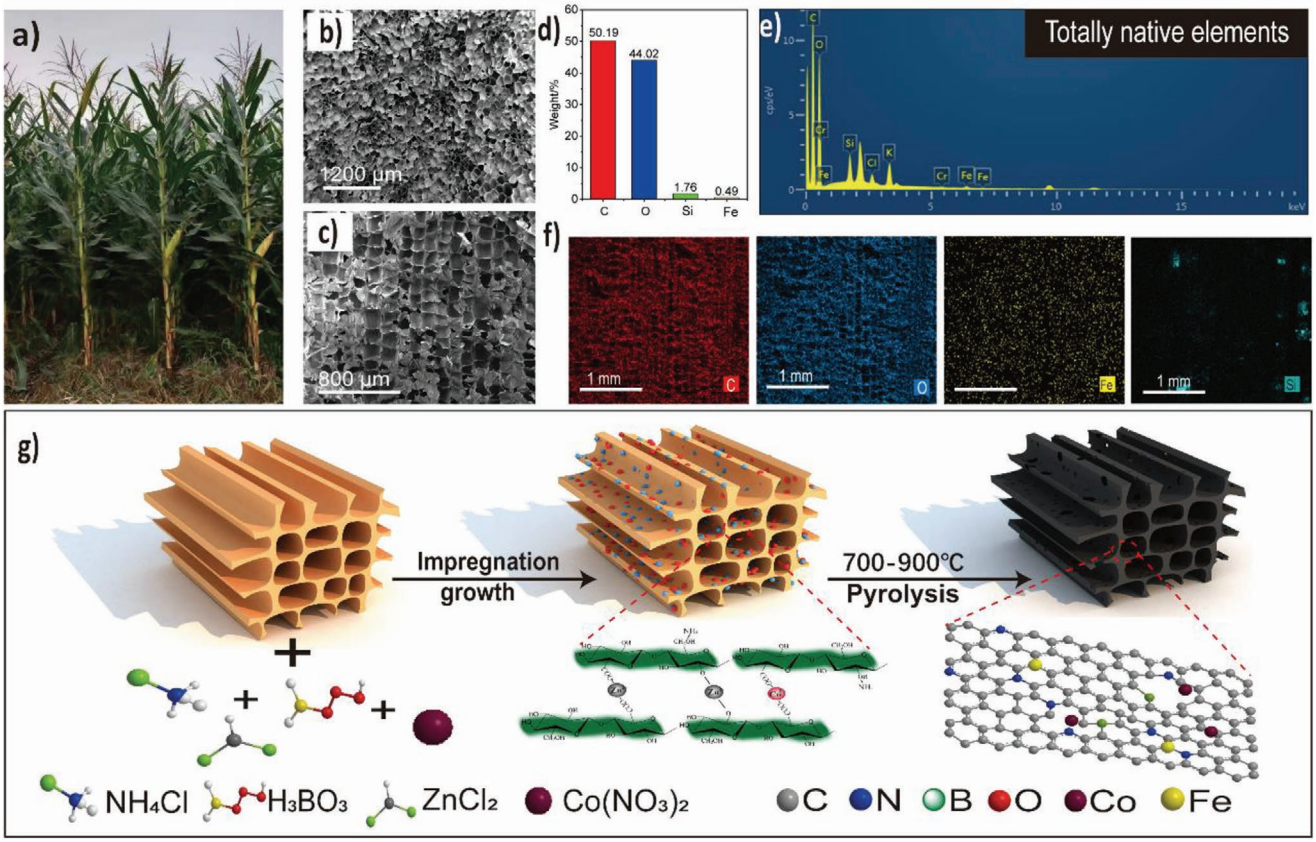


**Figure 1.** a) Picture of corn crops. b,c) SEM images of microstructures on cross section (upper) and longitudinal section (bottom) of the native cornstalks. d,e) Totally native elements within the cornstalks. f) EDS images of C, O, Fe, Si distribution in cornstalks. g) Schematic illustration of the synthesis methods for ORR/OER catalysts.

44.02 wt%) contents with the original wood (Figure 1d,e), implying their promise alternatives for other biomass resources of such wood. It also was found that the cornstalks comprise of native Si element (around 1.78 wt%) and transition metal Fe element (around 0.49 wt%) probably resulted from the process of corn's natural growth (Figure 1d–f). More importantly, the inherent advantages of the existing transition metal Fe element, are beneficial to generate more active sites for enhancing catalytic activities.

Figure 1g illustrated the schematic illustration of the synthesis methods for bifunctional ORR/OER electrocatalysts from the cornstalks. The objective of this work was that it provided a two-step strategy of initial hydrothermal reactions and subsequent carbonization process to fabricate electrocatalysts. The native cornstalks powders are pretreated by impregnation in aqueous $Co(NO_3)_2$, $ZnCl_2$, $H_3BO_3$, and $NH_4Cl$ followed by the hydrothermal reactions under 180 °C for 10 h, enabling the efficient dispersions and neighboring combination between active groups (e.g., rich hydroxyl) by doping $Co^{2+}$ and $Zn^{2+}$, both intra-pores and inter-pores. The resulted hydrothermal products were named as the HPs samples. The secondary carbonization process was performed at different temperatures of 700, 800, and 900 °C for 2 h which was defined respectively as the T-700, T-800, and T-900 samples. We used $ZnCl_2$ as the pore forming agent due to its easier pyrolytic evaporation in high-temperature carbonization process, which facilitates the generation of micropores and mesopores and also avoids the neighboring aggregations of transition metals. Additionally, the samples without the addition of $ZnCl_2$ carbonized at 800 °C were named as NP-T-800 samples and were also prepared for comparison by the same methods as abovementioned. In particular, $NH_3$ released from the unstable $NH_4^+$ expedites the cornstalks to decompose gradually in hydrothermal reaction and also the carbonization process (Figure 1g).

The comparative studies on the morphology of the native cornstalks, HPs, and T-800 samples were investigated respectively (**Figure 2**). Compared to the smooth surface of native cornstalks with petaloid-like structures (Figure 2a), the in situ grown particles with different morphologies of spherical (50 – 200 nm) or/and snowflake-like (10 – 100 nm) are clearly observed on the surface of HPs samples after hydrothermal reactions (Figure 2b). The pyrolytic vaporization of $Zn^{2+}$ further accelerates the corrosions and subsequently destroys the native microstructures of cornstalks in high-temperature carbonization processes. These were testified by clearly observing amounts of new micropores and mesopores on the surface of the T-800 samples (Figure 2c). Transmission electron microscopy (TEM) images further indicated significant mesoporous structural nature (Figure 2d). The edge-like graphitic structure was observed in the carbon skeleton revealing that the biochar materials resulted from cornstalks have promising electrical conductivities,[36] even under the probably negative effects resulted from discontinuous new pores. Traditionally, the transition metals of such Co and Fe deposited on the traditional carbon materials are easily aggregated under a high-temperature carbonizing process,[37] further weakening or even invalidating the catalytic activities. In contrast, the native cornstalks have rich hydroxyl and carboxyl group which enables the sufficient combination with neighboring metal ions in hydrothermal growth. As the deduction abovementioned, it was especially noted that $Zn^{2+}$ is deposited and grew within the porous cornstalks in hydrothermal reaction which also can serve as an efficient space isolator to disperse the neighboring Co and Fe metals.

The Energy-Fispersive X-ray Dpectroscopy (EDS) mapping images in Figure 2e demonstrated the uniform distributions of C, N, O, B, Co on the surface of the obtained T-800 samples. The results demonstrated that the present two-step strategy that possesses their ability to sufficiently disperse transition metals while operating in easily controlled environments. The comparative studies were investigated the influences of adding $ZnCl_2$ on the dispersions of Co, Fe. It was observed that the samples without $ZnCl_2$ caused significant aggregations of Co and Fe in high-temperature carbonization (Figure 2f,g). As one of the alternatives, the direct addition of $ZnCl_2$ in hydrothermal reactions enables huge nanopore production during high-temperature carbonization, and avoids Co and Fe aggregations, which provided a new effective pathway with metals dispersions (Figure 2h,k).

Fourier Transforms Infrared Spectroscopy (FTIR) was utilized to investigate the basic chemical bonding configurations of native cornstalks. It showed that the typical peaks of native cornstalks are located at 3457 and 1637 $cm^{-1}$, which attribute to stretching peaks of the –OH and C=O, respectively (**Figure 3**a). The band at 1061 $cm^{-1}$ is due to the C–O–C pyranose ring skeletal vibration. The results showed that cornstalks have rich hydroxyl group and carboxyl group, which conduce the effective chelation with metal ions.[38–39] The X-ray Photoelectron Spectroscopy (XPS) survey spectra further demonstrated the chemical structures of native cornstalks (Figure 3b). The high-resolution of C1s spectra is deconvoluted into three main peaks of C–C at 284.7 eV, C—O at 286.44 eV, and O—C=O at 288 eV, respectively. This result also verified the existence of hydroxyl and carboxyl group in the native cornstalks, which is consistent with the FTIR results. The corresponding X-ray diffraction (XRD) patterns of T-800 samples are displayed in Figure 3c. It indicated that there are two strong broad diffraction peaks centered at $2\theta = 23.5°$ and 43°, corresponding to the (002) and (100) crystal planes of graphitized carbon, respectively. However, it can be problematic that there is unconspicuous Co, Fe-containing phase peak in the XRD spectra, which is probably attributed to the much lower content in native cornstalk.[40] The graphitization and defect degree of the T-700, T-800, and T-900 samples were examined by Raman spectroscopy. Figure 3d typically displays two obvious peaks at 1348 and 1584 $cm^{-1}$ corresponding to carbon structures, indicating the defective/disordered carbon (D band) and the crystallized graphitic carbon (G band), respectively. Specifically, the relative intensity ratio of the D band and G band ($I_D/I_G$) reflects the graphitization and defect degree of carbon materials.[41] The T-700, T-800, and T-900 samples were prepared through high-temperature carbonization, in which a broader 2D peak appeared at around 2800 $cm^{-1}$, indicating a higher degree of graphitization. The comparative studies on $I_D/I_G$ intensity ratios of T-700, T-800, and T-900 samples are 1.22, 1.13, and 0.96, respectively. When increasing carbonization temperature, the degree of graphitization becomes much higher, indicating the changes of carbon structure leading to graphitizing

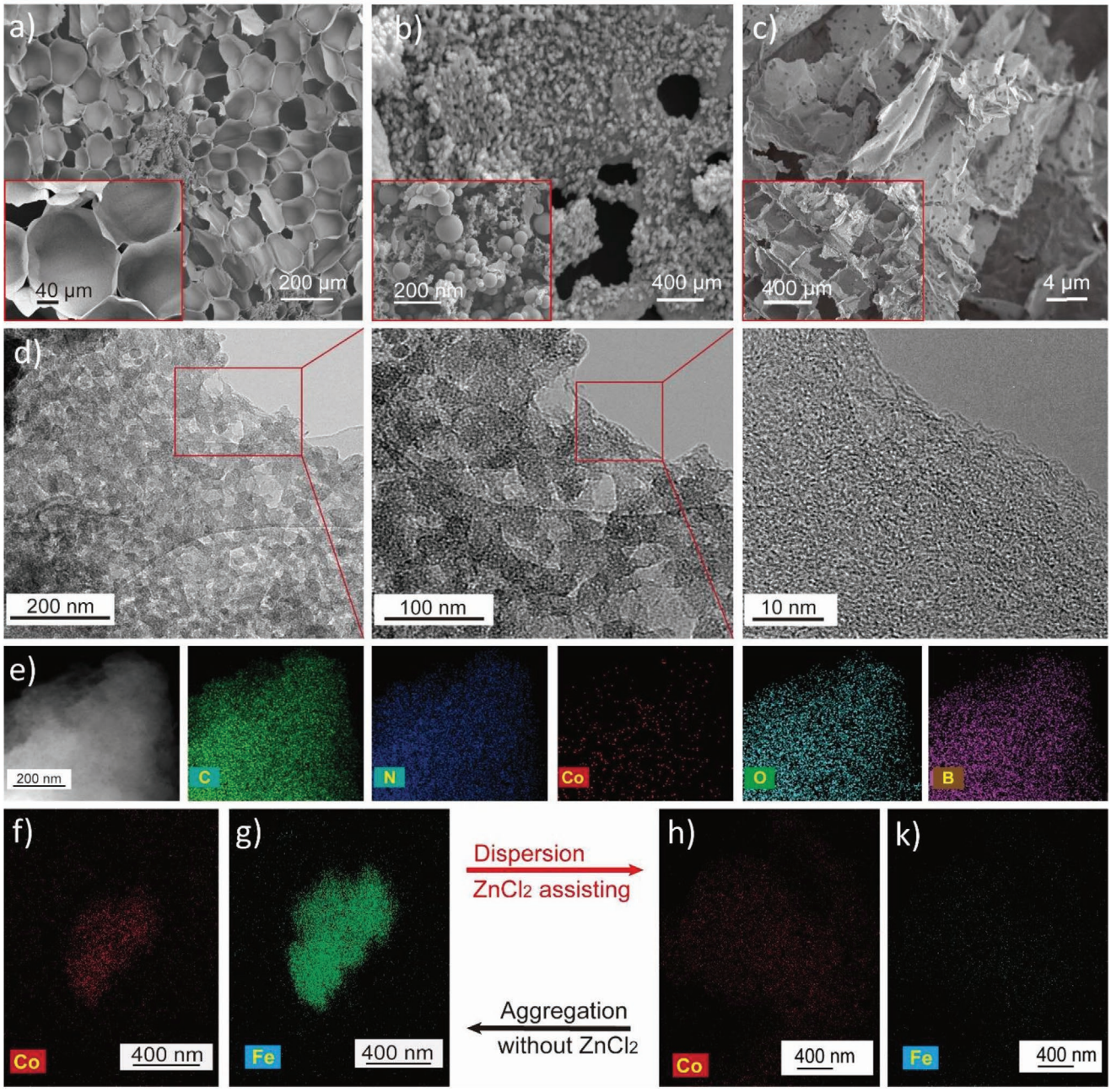


**Figure 2.** a–c) SEM images of native cornstalks (left), HPs (middle) and T-800 samples (right). d) TEM mapping images of T-800 samples with magnification by 200, 100, and 10 nm scale bar respectively. e) EDS mapping images of T-800 samples corresponding to the element distribution of C, N, Co, O, B respectively. f,g) EDS mapping images of aggregation of Co (left), Fe (right) without addition of $Zn^{2+}$ after 800 °C carbonization process. h,k) Perfect dispersions of Co (left), Fe (right) with addition of $ZnCl_2$ in carbonization process at 800 °C.

occurrence. The results demonstrated that the graphitization of the porous bio-char was intensified as the carbonization temperature increased. At the same time, the higher degree of graphitization is beneficial for enhancing the catalytic activities.[42]

The quest for both higher specific surface areas and suitable pore structures is perpetual in advanced electrocatalysts design. The specific surface area and pore volume were investigated by Brunauer–Emmett–Teller (BET) method with the typical nitrogen adsorption-desorption isotherms. As shown in Figure 3e, the isotherm curves are assigned to the typical type IV patterns with an obvious hysteresis loop at $P/P_0$ = 0.4 – 1.0, indicating the characteristics of both micropores and mesopores in carbonized samples. It was also revealed that the T-800 samples showed a much higher BET surface area of around 941.0 $m^2\ g^{-1}$ than that of NP-T-800 (around 530.0 $m^2\ g^{-1}$) without $ZnCl_2$ addition, indicating that $ZnCl_2$ not only disperses efficiently metal ions, but also significantly increases the specific surface areas due to the generation of abundant micropores and mesopores in carbonization process (Figure 2c). The results in the further studies confirmed

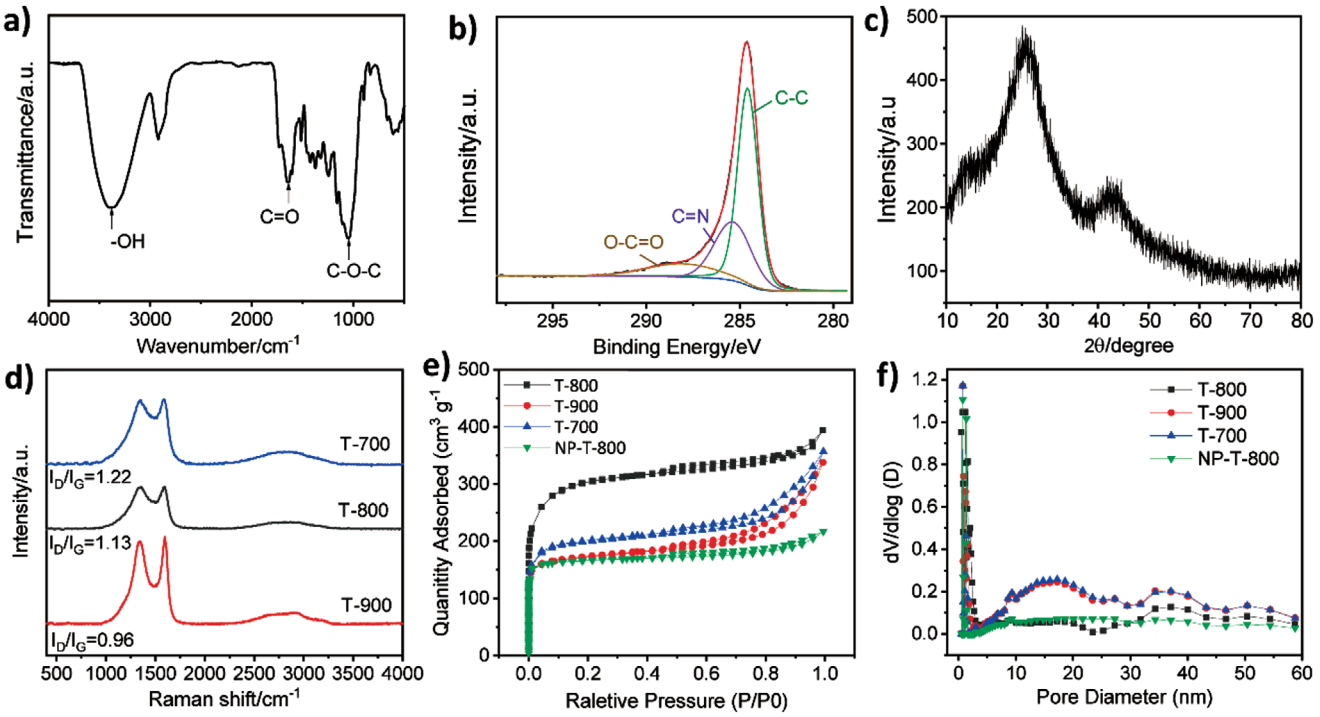


**Figure 3.** a) FTIR spectra of native cornstalks. b) High-resolution $C1_s$ spectra of cornstalks. c) XRD patterns of T-800 samples. d) Raman spectra of carbonized samples at various temperatures ($T = 700$, 800, and 900 °C). e) $N_2$ adsorption – desorption isotherms. f) Pore size distributions based on the BJH method for the different samples ($T = 700$, 800, and 900 °C).

that 800 °C is a promising carbonization temperature for promoting the specific surface areas, outperformed those at higher 900 °C or lower 700 °C (Figure 3e). The carbonized structures basically retained the native anisotropic morphology of the cornstalks, but created much more nanopore structures on the cell walls, showing a smaller pore size owing to the collapse and shrinkage in pyrogenic decomposition. In all cases by varying carbonization temperature, the pore size of the obtained samples generally ranges from 0.5 to 0 nm (Figure 3f), indicating the basic characters of micropores and mesopores. However, it still showed a much higher specific surface areas at 800 °C carbonization temperature. Notably, the nanometer-scale distribution of electrocatalyst centers on the electrode surface with abundant specific surface areas mostly contributes to obtain ORR or/and OER electrocatalytic activities. The previous reports had demonstrated that mesopore could provide effective channels for ion transport and thus enhances the transferring rate. Moreover, micro- and nanopore mainly offers more active sites for the storage of electrolyte ions. 3D hierarchical porous structure within biochar with high specific surface areas and abundant defect sites, is of special interest due to its potential for promoting electrocatalytic performances.[26] Our study sets out with a broad exploration of a kind of suitable biochar materials from cornstalks production, and the structure–composition–activity relationship of the selected materials was investigated by doping transition metals and heteroatoms under different preparation conditions.

The surface chemistry and the valance state of various elements in T-800 samples were scrutinized by XPS. The full spectra of the samples indicated the coexistence of C (75.85 at%), N (5.79 at%), B (2.04 at%), O (15.56 at%), and Co (0.58 at%) in the cornstalks with the native Fe (0.18 at%) (**Figure 4**a). Figure 4b indicated that the C1s spectrum is deconvoluted into three peaks of C–C at 284.6 eV, C=N at 285.4 eV, and O–C=O at 288.4 eV, respectively. The existence of the C=N bond further confirmed the successful incorporation of N into the cornstalks, which is emerging as an effective alternative for providing more active sites and $O_2$ adsorption sites. The high-resolution XPS spectrum of Co 2p exhibit two dominating peaks with binding energy at 780.2, 794.8 eV, corresponding to Co $2p_{3/2}$ and Co $2p_{1/2}$, respectively (Figure 4c). The Co 2p spectra can be classified into three characteristic peaks of $Co^0$ (779.2 eV), $Co^{3+}$ (780.2 eV), and $Co^{2+}$ (782.9 eV).

After pyrolytic evaporation of $NH_3$ from $NH_4^+$ in carbonization process, the resulted N content in the T-800 samples increased significantly, indicating the N-doping structures of biochar from cornstalks were expected, leading to a high 5.79% N content occurrence. For N 1s spectrum, it can be deconvoluted into four peaks, indicating pyridinic-N (398.2 eV), Co-Nx (399.4 eV), pyrrolic-N (400.9 eV), and graphitic-N (401.9 eV), respectively (Figure 4d). To improve their electrocatalytic activities for ORR and OER,[43] and ultimately realize the technical expectation of bifunctional ORR/OER catalysts, it is imperative to understand the effects of pyridinic N and graphitic N. The pyridinic N is often associated with promoting onset potential, while the graphitic N is associated with facilitating the four-electron transfer paths.[44] The previous literatures had verified that the formation of Co-N groups plays a key role in enhancing both the ORR and OER electrocatalytic activities.[45] In addition, Figure 4e showed that B 1s spectrum is deconvoluted into

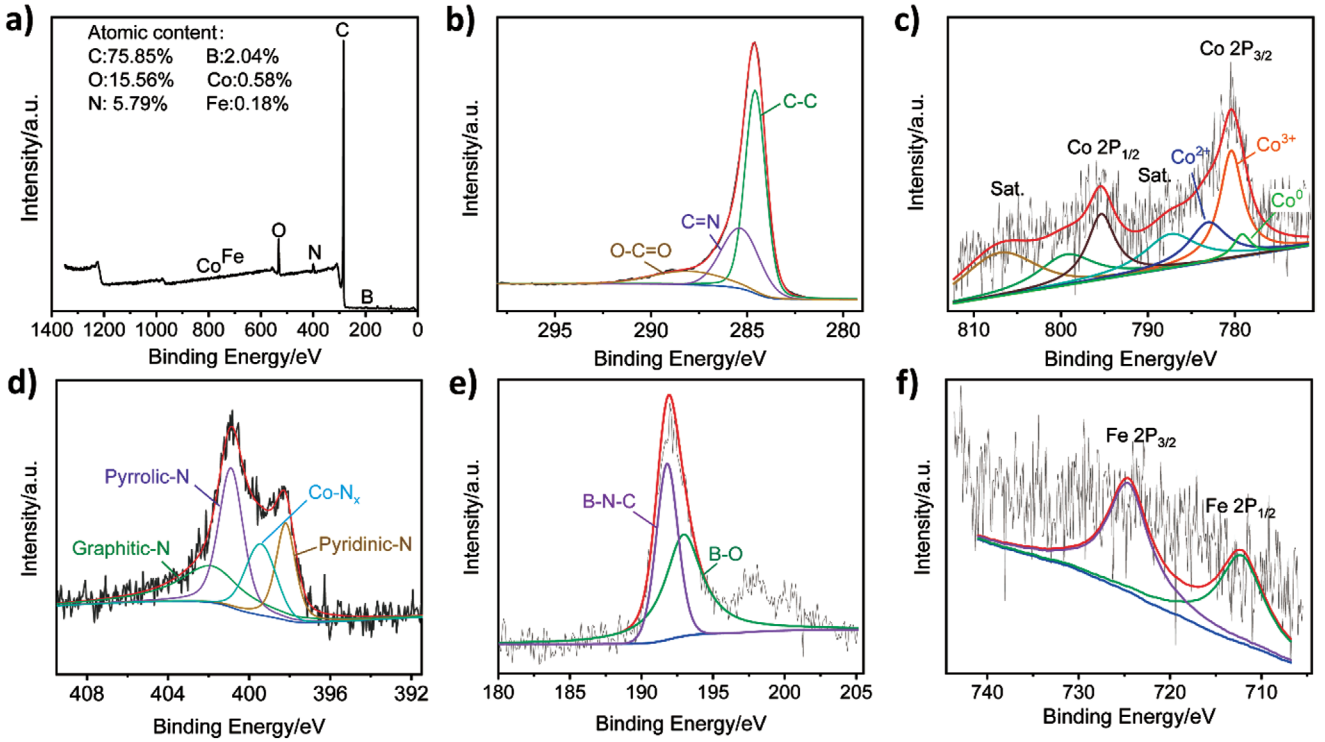


**Figure 4.** High-resolution XPS spectra of T-800 samples with a) full spectra, b) C 1s, c) Co 2p, d) N 1s, e) B 1s, f) Fe 2p.

two distinct peaks of B–N–C and B–O species, at 191.78 and 192.98 eV, respectively. As shown in Figure 4f, the observation of peak existence of Fe from native cornstalks without artificially doping is also conducive to improve the electrocatalytic activities.

### 2.2. Electrochemical Characterizations

The ORR performances of our catalysts and the commercial Pt/C (20 wt%) were comparatively investigated in the same $N_2$- or $O_2$-saturated 0.1 M KOH using a typical three-electrode system at room temperature. Cycle Voltammetry (CV) measurements were performed to study the behaviors of T-800 samples, and the commercial Pt/C electrodes in $N_2$- and $O_2$-saturated electrolytes, respectively. It should be noted that it tolerates the almost no absence of oxygen reduction peak in $N_2$-saturated electrolyte while arising significant peak in the $O_2$-saturated electrolyte, which appears closer to positive location than the commercial Pt/C catalysts (**Figure 5**a). These results implied that ORR catalytic reaction is highly intensified in the T-800 samples under the same $O_2$-saturated electrolytes, because oxygen reduction via the Co, Fe, B, N doping requires not only the mesoporous structures, but also the synergetic effects of sufficient active sites and $O_2$ adsorption sites within biochar structure from cornstalks. In a further study by Linear Sweep Voltammetry (LSV) measurements demonstrated that 800 °C carbonization temperature is favored at achieving the best ORR catalytic activity, with the most positive half-wave potential ($E_{1/2}$) of 0.857 V, much higher than those samples at 700 and 900 °C. It is ascribed to the appropriate carbonization process that facilitates the formation of Co, Fe, B, N-doping active sites in the efficient pyrolytic mesoporous structures (Figure 5b). As the above demonstrated pyrolytic evaporation of $ZnCl_2$ exhibited significant impacts on the specific surface areas and carbonous structures, further investigations were carried out to achieve a fundamental understanding of its influences on ORR catalytic activity. The NP-T-800 samples without $ZnCl_2$ doping, however, exhibits unsatisfactory ORR performance with a lower half-wave potential of 0.782 V. It generates a perfect half-wave potential superior to the commercial Pt/C (0.834 V) when doped $ZnCl_2$. In a conclusion, the experimental results guaranteed the outstanding ORR performances of T-800 samples and ensured its capability as a nonnoble but cost-effective ORR electrocatalyst for practical applications.

In order to understand the ORR kinetics, LSV curves were further compared for different rotating speeds (Figure 5c). The Kentucky–Levich (K–L) plots display distinctly linear tendency at different electric potentials from 0.2 to 0.7 V, demonstrating a typical first order kinetic process (Figure S1, Supporting Information). The calculated electron transfer number is closer to 4.0 conforming to a pathway of four-electron reaction. Figure 5d showed the Tafel curves from experiments in which the T-800 samples have much lower Tafel slope of 95.01 mV $dec^{-1}$ than 105.43 mV $dec^{-1}$ of the commercial Pt/C. The results suggested that the electron transfer efficiency and catalytic kinetics of the ORR catalytic reaction are highly intensified due to the synergistic contributions from nonmetal N, B and transition metal Co, Fe in unique 3D porous biochar structures. But it's important to know that the NP-T-800 samples without $ZnCl_2$ addition showed higher Tafel slope of 103.2 mV $dec^{-1}$ closing to the commercial Pt/C.

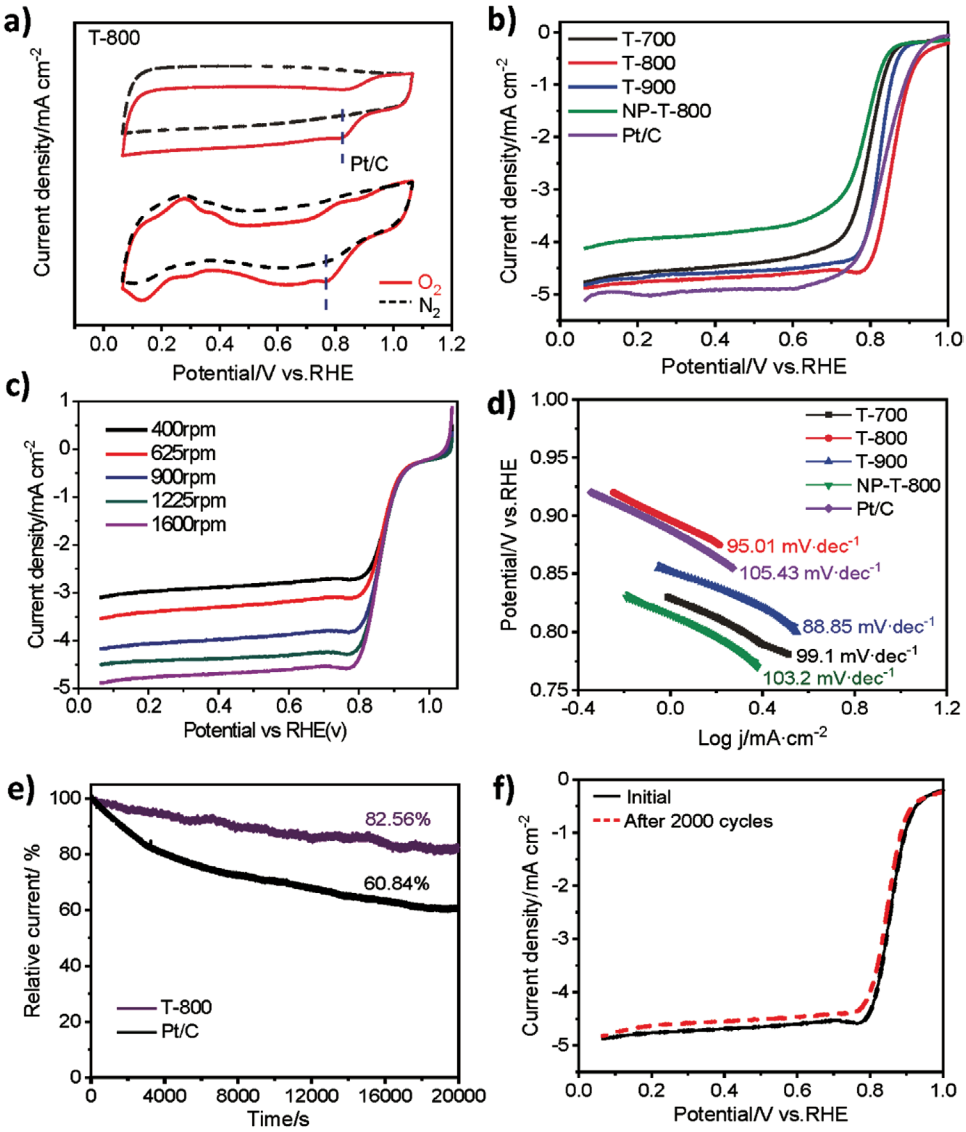


**Figure 5.** a) CV curves of the T-800 samples, and commercial Pt/C. b) LSV curves of 20 wt% commercial Pt/C and the electrocatalysts with different temperatures and $ZnCl_2$ addition for comparison (at 1600 rpm in $O_2$-saturated 0.1 M KOH, respectively). c) LSV curves of T-800 samples at different rotation rates. d) Tafel slopes of 20 wt% commercial Pt/C and the electrocatalysts. e) Current–time chronoamperometric measurements of T-800 samples and the commercial Pt/C through 20 000 s cycle stability tests. f) LSV curves of the T-800 samples before and after 2000 cycles in 0.1 M KOH.

The evaluation of ORR durability is currently a matter of intensive concerns due to its vital importance to scale up for practical applications. After testing ORR stability with CV scanning for 2000 cycles, the T-800 samples electrocatalyst only displayed a slight decrease in LSV curves (Figure 5e). Current–time (*i*–*t*) chronoamperometric measurements were carried out for evaluating its stability behaviors for ORR activities. It was also found that after 20 000 s cycle stability tests, the electrocatalysts still maintained at higher 82.56% relative current, superior to 60.83% of the commercial Pt/C.

The inevitable structural defects in the Co-Fe, B-N-doped biochar matrix could act as OER active sites to enhance catalytic activities, besides the ORR activity. To demonstrate the OER performances of our electrocatalysts, various investigations were performed by using a three-electrode system with 1.0 M $O_2$-saturated KOH solution. As shown in **Figure 6**a, the T-800 samples carbonized at 800 °C showed the superior OER activity with the lowest overpotential of 383 mV at the current density of 10 mA $cm^{-2}$, much lower than that at 700 °C (474 mV), and at 900 °C (415 mV). However, the NP-T-800 samples without the incorporated $ZnCl_2$ have a much higher overpotential of 456 mV at the current density of 10 mA $cm^{-2}$. The results further demonstrated that the effective and convenient method to deal with $ZnCl_2$ displays a vital role in achieving bifunctional ORR and OER performances. The overpotential of the electrocatalysts is still competitive, in spite of its slightly larger than the commercial $IrO_2$ catalyst (343 mV). However, it is worth noting that the T-800 samples generated a current density of 114 mA $cm^{-2}$ at 1.9 V (vs RHE), which is almost equal to the commercial $IrO_2$ catalyst (114 mA $cm^{-2}$) (Figure 6a).

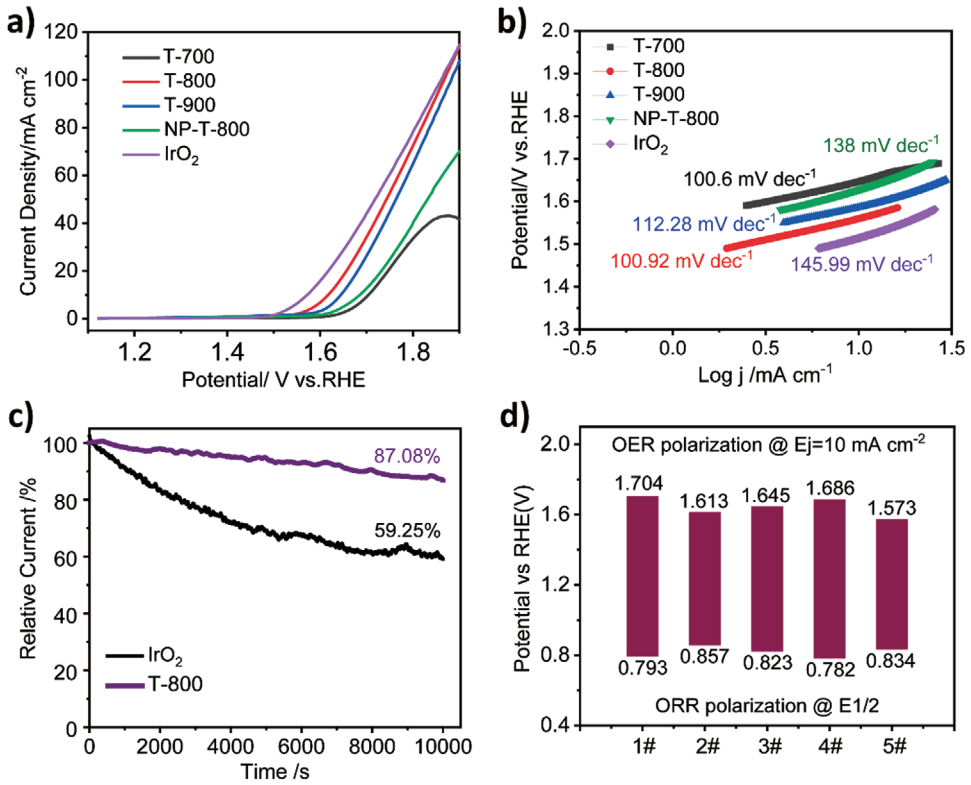


**Figure 6.** a) LSV curves of T-700, T-800, T-900, NP-T-800, and commercial $IrO_2$/C in 1 M KOH. b) Tafel slopes of T-700, T-800, T-900, NP-T-800, and commercial $IrO_2$/C. c) *i–t* chronoamperometric responses of T-800 and $IrO_2$/C. d) Polarization curves of as-prepared catalysts for bifunctional catalytic activity, 1# stands for T-700, 2# stands for T-800, 3# stands for T-900, 4# stands for NP-T-800, and 5# stands for the commercial Pt/C and $IrO_2$.

To reveal the catalytic kinetics in the OER activities, and further verify the contribution in improving oxygen utilization in the Co-Zn, B-N-doped biochar matrix, we conducted comparative experiments under different carbonization temperatures. Figure 6b indicated that all the samples showed similar Tafel slopes around 100 mV $dec^{-1}$, lower than that of $IrO_2$ (145.99 mV $dec^{-1}$) and the NP-T-800 (138 mV $dec^{-1}$), demonstrating them with favorable OER kinetics. We measured the current–time (i–t) chronoamperometric measurements of the T-800 samples to evaluate their stability. Figure 6c illustrated that the stability of the T-800 samples still maintains about 87.08%, whereas that of the commercial $IrO_2$ decreases to 59.25% after 10 000 s times. The results also testified that the T-800 performed better durability than the commercial $IrO_2$ catalyst in alkaline electrolytes.

The further evaluations were investigated by comparing the potential differences between OER and ORR (noted as $\Delta E = E_{j=10} - E_{1/2}$, $E_{j=10}$ which represents the potential required to generate a current density of 10 mA $cm^{-2}$ for OER) (Figure 6d). The results implied that the T-800 samples showed the smallest potential difference of 0.756 V $\Delta E$ showing an excellent bifunctional electrocatalytic activities for both ORR and OER requirements, while the NP-T-800 samples without the addition of $ZnCl_2$ displayed a much higher potential difference ($\Delta E$ = 0.904 V).

Compared the previously reported ORR/OER electrocatalytic activities with the commercial Pt/C and $IrO_2$, respectively, the Co-Fe, B-N-doped biochar matrix shows advantages of: 1) using agricultural waste of cornstalks without fossil fuel consumptions; 2) being eco-friendly doping process without organic compounds and noble metals use, and wastes releasing; 3) utilizing the 3D porous biochar structure within cornstalks; 4) possessing high-performance bifunctional ORR/OER catalytic activities with outstanding working stability compared to the commercial Pt/C and $IrO_2$ catalysts, and 5) having low production cost with sustainability for large-scale fabrications.

### 2.3. Computational Analysis

It was theoretically demonstrated the fact that valuable synergistic contributions from nonmetals and transition metals significantly enhance the ORR/OER activities by the computational method of Vienna Ab Initio Simulation Package (VASP) on the basis of the density-functional theory (DFT). Initially, we constructed pure graphene with 80 carbon atoms in total, then introduced Co, N, B co-doping into the graphene, and the optimized structures exhibit minor curvature, indicating typical graphene in ambient condition (**Figure 7**).

Graphene doped with Co atoms far away and with Co atoms close to each other are denoted as Co-far-away and Co-close in this work. It can be seen from **Figure 8** that Co-far-away and Co-close showed distinct characteristics in both OER and ORR. For example, the Co-close binds hydroxide strongly indicated by a large negative $\Delta G$ of –1.20 eV, and the OH bonds with two Co

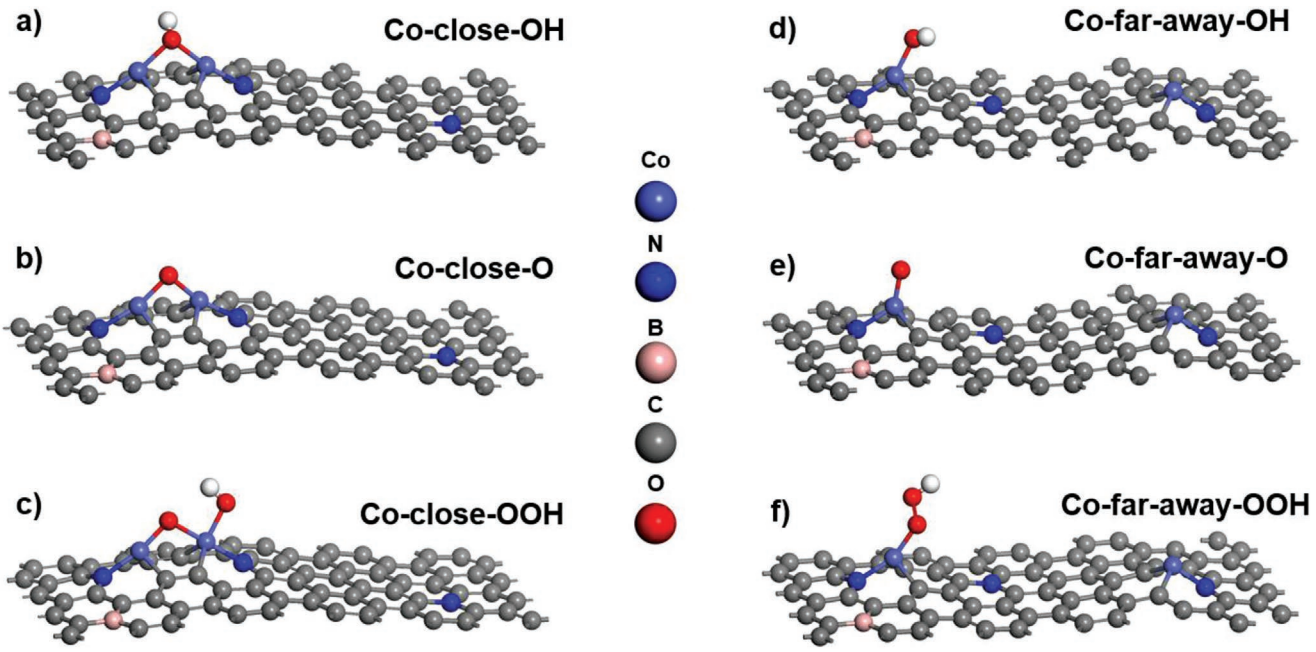


**Figure 7.** Relaxed heterostructures of a) pure $Ni_3S_2$-NiOOH and b) pure $Ni_3S_2$-NiOOH with S vacancy, c) Fe-doped $Ni_3S_2$-NiOOH and d) Fe-doped $Ni_3S_2$-NiOOH with S vacancy.

atoms in the same hexagon carbon ring tightly in OER (Figures 7a and 8a).

This scenario is detrimental to OER reaction, and the tight bonding between Co and OH overcomes large amounts of energy to release $O_2$ in the latter step. And the calculated results further confirmed our previous assumption with a gigantic energy barrier in the last step of 5.06 eV (Equation (1d)). In the same way, the determining overpotential of OER for Co-close is calculated to be 3.83 V (Figure 8a).

Whereas, Co-far-away achieved more thermal neutral initial absorption of hydroxide (–0.35 eV), which is about ¼ compared with that of Co-close (Figures 7d and 8a). The determining step occurs when Co-far-away absorbs the second hydroxide on O*, and it shows an energy barrier of 2.74 eV, rendering a determining overpotential of 1.51 V less than half of that in Co-close (3.83 V) (Figures 7e,f and 8b). In terms of ORR, Co-far-away also exhibits better performance than Co-close. Although Co-close bonds $O_2$ effortlessly compared with Co-far-away (–3.83 eV vs –0.79), Co-far-away outperformed Co-close in their common determining step – desorption of OH (Equation (2d)). Specifically, Co-close only requires an overpotential of 1.58 V compared with Co-far-away (2.43 V), which is 35% less energy required (Figure 8).

For OER process, we investigated the active sites on the surface of doped graphene by calculating the total energies of OH intermediate adsorbed on five different sites on the catalyst

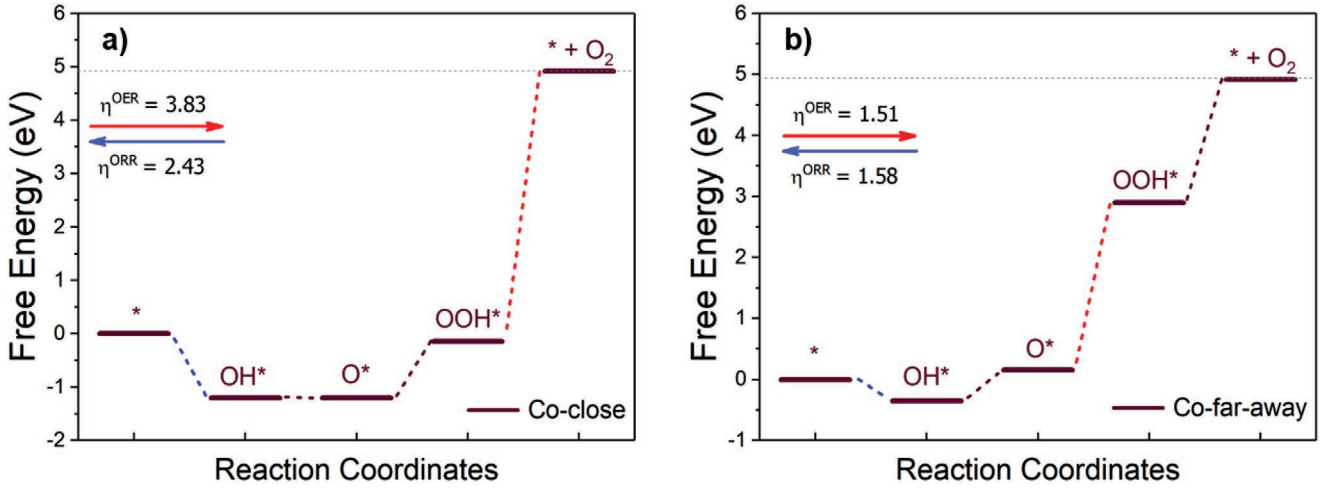


**Figure 8.** Calculated ORR and OER reaction coordinates of doped graphene with a) Co atoms far away from each other and b) Co atoms close to each other.

surface (Figure S2, Supporting Information). The five possible OH adsorption sites are: 1) bridge between N and Co, 2) center of hexagon, 3) top of Co, 4) top of N, and 5) top of B. In the context, we denote graphene doped with Co-close pattern as G-Co-close, and graphene doped with Co-far-away as G-Co-far-away. We found that, after optimization, Co site in both G-Co-far-away and G-Co-close is the major active site for OER to initiate due to the lowest calculated total energies of –729.47598 (Figure S2b, Supporting Information) and –731.13024 eV (Figure S2i, Supporting Information), as also shown in Table S1 (Supporting Information). It was also found that the calculated total energies of OH on Boron gives relatively larger value than that on Co, which means B site is not an active site compared to Co. For ORR process, we conducted similar calculation and found that Co is the main adsorption site of $O_2$ molecule for both G-Co-far-away and G-Co-close, with lower energies than that on Boron (Table S1, Supporting Information). Specifically, G-Co-far-away gives –729.86274 eV on Co, which is lower than –726.87536 eV on Boron (Figure S3a,b: Supporting Information); meanwhile, G-Co-close gives –731.46475 eV on Co, which is lower than –727.70228 eV on Boron (Figure S3c,d: Supporting Information). Interestingly, G-Co-close binds intermediates of OH and $O_2$ stronger than G-Co-far-away counterpart, which would position the catalytic active Co sites in G-Co-close. Other than the porous structures with large surface areas, and high graphitization degrees. It was identified the metal and non-metals doping account for the outstanding performance in our catalysts. We conducted partial density of states to elucidate the mechanism (Figure S4, Supporting Information). We also found that, for G-Co-far-away, d band electrons in Co contribute major carrier density around the Fermi level, whereas, p electrons in C and N only account for small amount of free carrier density (Figure S4a, Supporting Information). The p electrons contributed by Boron is even less indicated by the flat spectrum around Fermi level. For G-Co-close, similar trend was observed, Co accounts for major carrier density among other types of atoms around Fermi level (Figure S4b, Supporting Information). Interestingly, free carrier density from Co, N and C in G-Co-far-away show higher peaks than that in G-Co-close, which means G-Co-far-away shows overall better conductivity than G-Co-close.

In summary, Co-far-away outperformed Co-close due to the moderate adsorption and desorption energy of OH intermediates. In comparison, strong adsorption of OH in Co-close poisons the catalytic sites in OER, and also hinders the release of OH in ORR. The calculated results reveal the mechanism behind the outstanding OER/ORR activities of Co-far-away with successfully achieving Co separation for enhancing their performances.

## 3. Conclusions

In summary, we have successfully fabricated high-performance bifunctional ORR/OER catalysts made of agricultural wastes of cornstalks with perfect working stability. The synergetic effects of sufficient active sites and $O_2$ adsorption sites in biochar structures were highly intensified by incorporating transition metals of Co and Fe, and heteroatom N, B through a facile hydrothermal treatment and carbonization process (800 °C). It was especially noted that pyrolytic evaporation of $ZnCl_2$ in carbonization process not only prevents the neighboring aggregations of Co and Fe in carbonization process, but also increased the specific surface areas with creating abundant smaller micropores and mesopores structures. Those results produced more active sites for oxygen diffusion and electrolyte ions transfer, significantly enhancing the ORR and OER performances. Our catalysts derived from the native cornstalks possessed competitive bifunctional ORR and OER performances, perfect stabilities and also promise cost-effectiveness compared to the commercial Pt/C and $IrO_2$. These findings accelerate the developments of next-generation of biochar-based bifunctional electrocatalysts with sustainability and eco-system.

## 4. Experimental Section

*Materials*: All chemicals were obtained from commercial sources and used without further treatments, which is listed as follows: the cornstalks were obtained by collecting from farmland in Shandong Province, Cobalt nitrate hexahydrate ($Co(NO_3)_2 \cdot 6H_2O$, ≥99%), Zinc chloride ($ZnCl_2$, ≥98%,) and Potassium hydroxide(KOH, ≥85%) were purchased from Aladdin Industrial Corporation, boric acid ($H_3BO_3$, ≥99.5%) and ammonium chloride ($NH_4Cl$, ≥99.5%) were purchased from Shanghai Macklin Biochemical Co., Ltd, China. Ethanol ($C_2H_5OH$, ≥95%) and Hydrochloric acid (HCl, 36–38%) were obtained by Guangzhou chemistry Co., Ltd, China, Nafion (20 wt%) were purchased by American DuPont (China) Co., Ltd.

*Hydrothermal Reaction*: Typically, the pristine cornstalk particles were milled by a ball mill, followed by sieving through 60 mesh to obtain cornstalk powders without further purification process. 1.50 g $Co(NO_3)_2 \cdot 6H_2O$, 3.00 g $ZnCl_2$, 1.00 g $H_3BO_3$, and 5.00 g $NH_4Cl$ were completely dissolved in deionized water, respectively. And then, 1.00 g cornstalk powder was poured into the above solution with a mixing process for the initial 2 h, and subsequently stirred for at least 12 h at room temperature. After completing the mixing process, the resulting mixtures were sealed in an autoclave reactor for a hydrothermal reaction carried out at 180 °C for 10 h. Once 10 h had elapsed, the reaction product was air-cooled down to room temperature. The pretreated samples were repeatedly washed with deionized water to remove residuals. Then, the vacuum-drying process was carried out at 60 °C for at least 10 h. The resulted powder samples were named hydrothermal precursors (HPs).

*Carbonization Process*: Subsequently, $NH_4Cl$ was again required for treating HPs samples before the carbonization process. A mixture of 1:3 mass ratio of $NH_4Cl$ and deionized water was stirred to completely dissolve. The $NH_4Cl$ solution was adequately mixed with the HPs samples. Then, another vacuum-drying process was carried out at 120 °C until the treated HPs samples were obtained. The carbonation process was performed at different temperatures (700, 800, and 900 °C) for 2 h in a nitrogen atmosphere. After completing the carbonization process, the resulting samples were etched with 1.00 M hydrochloric acid solution for 12 h at room temperature, followed by the repeated centrifugation for washing with excess deionized water. After drying at 80 °C for another 12 hours, the T-700, T-800, T-900 electrocatalysts were obtained respectively. Furthermore, NP-T-800 samples were also prepared for comparison by the same methods as abovementioned without the addition of $ZnCl_2$.

*Characterizations*: X-ray diffraction (XRD) patterns of 10–80° were measured by a Rigaku diffractometer (D/MAX/IIIA, 3 kW) under 40 kV. Raman spectra were recorded on a Renishaw in Via Raman microscope with an Arion laser at the excitation wavelength of 514.5 nm. The microstructures and morphologies of the native cornstalks, HPs and T-800 samples were observed by field-emission scanning electron microscopy (FE-SEM Merlin, Zeiss) at an acceleration voltage of 5 kV and transmission electron microscopy (TEM) (JEM2100F) at an acceleration

voltage of 200 kV. The Rucker Vector33 spectrometer was used to record the Fourier transform infrared (FTIR) spectra of the obtained samples. The Brunauer-Emmett-Teller (BET) specific surface area and porous structure were measured at 77 K by using a Micromeritics ASAP 2020 system. The X-ray photoelectron spectroscopy (XPS) of the sample was measured by Kratos Axis Ultra DLD electron spectrometer, all dates were corrected using the C1s peak at 284.6 eV as an internal standard.

*Electrochemical Tests*: The three-electrode system were carried out on the CHI 760E Electrochemical Workstation (CH Instrument, Shanghai). The prepared catalyst was coated on the glassy carbon rotating disk electrode (RDE) as the working electrode, while the Hg/HgO electrode was the reference electrode. A graphite rod served as the counter electrode for ORR and OER tests. The catalyst ink was prepared by ultrasonically dispersing 5 mg the as-prepared catalysts (including reference catalysts: commercial Pt/C catalysts) in 1 mL of a mixed solution containing 0.98 mL of ethanol/water (1:1, v/v) and 20 mL of 20 wt% Nafion solution for 30 min. Then, 10 µL catalyst ink was subsequently pipetted onto the surface of a glassy carbon electrode surface and dried at room temperature. Cyclic voltammetry (CV) experiments were carried out in $N_2$/$O_2$ saturated 0.1 M KOH solution at a scan rate of 10 mV $s^{-1}$ at room temperature. The ORR test was performed by linear sweep voltammetry (LSV) in $O_2$ saturated 0.1 M KOH (pH = 13) solution at a rotating rate of 1600 rpm with a scan rate of 5 mV $s^{-1}$ at room temperature, where the potential range is 0.2 – 1.1 V (vs RHE). The long-term stability evaluation of the T-800 and Pt/C for ORR was determined at a constant voltage of 0.6 V versus Hg/HgO in $O_2$ saturated 0.1 M KOH electrolyte at a rotation speed of 1600 rpm. OER measurements were carried out by loading the catalyst on carbon paper (1 × 1 cm) with a load of 0.5 mg $cm^{-2}$ at a scanning rate of 5 mV $s^{-1}$ in $O_2$ or $N_2$ saturated 1.0 M KOH (pH = 14). The long-term stability evaluation of the T-800 and $IrO_2$ for OER was determined at a constant voltage of 0.383 V versus Hg/HgO. The electron transfer number (n) can be evaluated by Koutecky–Levich (K-L) equation:[17]

$$\frac{1}{J}=\frac{1}{J_k}+\frac{1}{J_d}=\frac{1}{B\omega^{1/2}}+\frac{1}{J_k} \tag{1}$$

Where $J$ is measured current, $J_d$ is the diffusion-limiting current, $J_k$ is the kinetic current, and $\omega$ is the electrode rotating rate. $B$ is the slope of Koutech-Levich (K-L) plots, and the calculation formula is as follows:

$$B=0.62nFC_oD^{\frac{2}{3}}\nu^{-\frac{1}{6}} \tag{2}$$

Where $n$ stands for the electron transfer number, $F$ stands for the Faraday constant (96 485 C $mol^{-1}$), $C_o$ stands for the $O_2$ concentration in liquid ($1.2\times10^{-3}$ mol $cm^{-3}$), and $D$ stands for the $O_2$ diffusion coefficient ($1.9\times10^{-5}$ $cm^2$ $s^{-1}$) in the 0.1 M KOH, $\nu$ stands for the kinematic viscosity (0.01 $cm^2$ $s^{-1}$).

*Computational Method*: In order to investigate the mechanism behind their ORR and OER catalytic activities, first-principles calculation were adopted to study the ORR and OER reaction pathways, involving Co, N, B co-doped graphene in two patterns of Co atoms far-away and closely arranged. The Vienna Ab Initio Simulation Package (VASP) with Projected Augmented Wave (PAW) scheme was used as the computational method[46] on the basis of the density-functional theory (DFT).[47–48] Besides, the Perdew–Burke–Ernzerhof Generalized Gradient Approximation (PBE-GGA) exchange and correlation functionals[49] were further investigated, in which the Monkhorsk-Pack k-point samples were served as 1 × 1 × 1 for optimization of pure Co, N, B co-doped graphenes,[50] and the cutoff energy of 500 eV was adopted throughout the relative calculations. Here, the OER via 4e⁻ pathways,[51–52] and the overall and elementary reaction steps were calculated and listed as following:

$$2H_2O(l)\rightarrow O_2+4H^++4e^- \tag{3}$$

$$H_2O(l)+*\rightarrow OH^*+e^-+H^+ \tag{3a}$$

$$OH^*\rightarrow O^*+e^-+H^+ \tag{3b}$$

$$H_2O(l)+O^*\rightarrow OOH^*+e^-+H^+ \tag{3c}$$

$$OOH^*\rightarrow O_2(g)+e^-+H^+ \tag{3d}$$

The ORR is the reverse reaction of OER,[52–56] which can be described via the reverse 4e⁻ pathways with the overall and individual steps as following:

$$O_2+4H^++4e^-\rightarrow 2H_2O \tag{4}$$

$$*+O_2(g)+e^-+H^+\rightarrow OOH^* \tag{4a}$$

$$OOH^*+e^-+H^+\rightarrow H_2O(l)+O^* \tag{4b}$$

$$O^*+e^-+H^+\rightarrow OH^* \tag{4c}$$

$$OH^*+e^-+H^+\rightarrow H_2O(l)+* \tag{4d}$$

where * stands for an adsorption site on co-doped graphene, l and g stands for liquid and gas phases, respectively.

The calculated Gibbs free energy differences ($\Delta G$) of each reaction step in OER and ORR are indicators of the energy barriers in each step involving one electron transfer, which can be expressed as following:

$$\Delta G=\Delta E+\Delta ZPE-T\Delta S \tag{5}$$

where ΔZPE and ΔS are the differences of zero-point energies and entropy of adsorbates (OH*, O*, OOH*), $\Delta E$ is the adsorption energy calculated as the following equations:

$$\Delta E(OH^*)=E(OH^*)-E(*)-E(H_2O)+1/2E(H_2) \tag{6}$$

$$\Delta E(O^*)=E(O^*)-E(*)-E(H_2O)+E(H_2) \tag{7}$$

$$\Delta E(OOH^*)=E(OOH^*)-E(*)-2EH_2O+3/2E(H_2) \tag{8}$$

where E($OH^*$), E($O^*$), and E($OOH^*$) are the total energies of catalyst adsorbed with OH, O and OOH, E($H_2O$) and E($H_2$) are the total energies of $H_2O$ and $H_2$.

Therefore, the OER pathways can be expressed as: $\Delta G_{1a}=\Delta G_{OH*}$, $\Delta G_{1b}=\Delta G_{O*}-\Delta G_{OH*}$, $\Delta G_{1c}=\Delta G_{OOH*}-\Delta G_{O*}$, $\Delta G_{1d}=4.92-\Delta G_{OOH*}$ the ORR pathways: $\Delta G_{2a}=\Delta G_{OOH*}-4.92$, $\Delta G_{2b}=\Delta G_{O*}-\Delta G_{OOH*}$, $\Delta G_{2c}=\Delta G_{OH*}-\Delta G_{O*}$, $\Delta G_{2d}=\Delta G_{OH*}$.[57–58]

The determining overpotential ($\eta$) can be calculated to indicate the largest energy barrier and the catalytic performance for OER and ORR:

$$\Delta\eta^{OER}=max\{\Delta G_{1a},\Delta G_{1b},\Delta G_{1c},\Delta G_{1d}\}/e-1.23 \tag{9}$$

$$\eta^{OER}=max\{\Delta G_{2a},\Delta G_{2b},\Delta G_{2c},\Delta G_{2d}\}/e+1.23 \tag{10}$$

## Supporting Information

Supporting Information is available from the Wiley Online Library or from the author.

## Acknowledgements

Y.L. and Y.Q. contributed equally to this work. This work was kindly supported by Guangdong Basic and Applied Basic Research Foundation of Guangdong Province (No. 2020A1515011013) and Science and Technology Planning Project of Guangdong Province (No. 2020A050515004), the Leading Talents of Guangdong Province Program (2016LJ06C536), Shenzhen Key Laboratory of Interfacial Science and Engineering of Materials (ZDSYS20200421111401738), Guangdong-Hong Kong-Macao Joint Laboratory (grant no. 2019B121205001), Basic Research Project

of the Science and Technology Innovation Commission of Shenzhen (No. JCYJ20200109141640095); and also was supported by the Science and Technology Development Fund from Macau SAR (FDCT) (0102/2019/A2, 0035 /2019/AGJ, 0154 /2019/A3, 0081/2019/AMJ, and 0033/2019/AMJ).

## Conflict of Interest

The authors declare no conflict of interest.

## Data Availability Statement

The data that support the findings of this study are available from the corresponding author upon reasonable request.

## Keywords

ORR/OER catalysts, porous cornstalks, synergistic effects, working stability, $ZnCl_2$

Received: September 19, 2021
Revised: November 1, 2021
Published online:

[1] D. Ji, L. Fan, L. Li, S. Peng, D. Yu, J. Song, S. Ramakrishna, S. Guo, *Adv. Mater.* **2019**, *31*, 1808267.
[2] S. Peng, X. Han, L. Li, S. Chou, D. Ji, H. Huang, Y. Du, J. Liu, S. Ramakrishna, *Adv. Energy Mater.* **2018**, *8*, 1800612.
[3] K. Wu, L. Zhang, Y. Yuan, L. Zhong, Z. Chen, X. Chi, H. Lu, Z. Chen, R. Zou, T. Li, C. Jiang, Y. Chen, X. Peng, J. Lu, *Adv. Mater.* **2020**, *32*, 2002292.
[4] Y. Yang, H. Fei, G. Ruan, L. Li, G. Wang, N. Kim, J. Tour, *ACS Appl. Mater. Interfaces* **2015**, *7*, 20607.
[5] Y. Nie, L. Li, Z. Wei, *Chem. Soc. Rev.* **2015**, *44*, 2168.
[6] F. Li, G. Han, H. Noh, S. Kim, Y. Lu, H. Jeong, Z. Fu, J. Baek, *Energy Environ. Sci.* **2018**, *11*, 2263.
[7] J. Diao, Y. Qiu, S. Liu, W. Wang, K. Chen, H. Li, W. Yuan, Y. Qu, X. Guo, *Adv. Mater.* **2019**, *32*, 1905679.
[8] S. Hu, J. Wang, J. Zhang, J. Lim, Y. Gao, S. Zhang, *Appl. Catal., B* **2021**, *282*, 119593.
[9] Q. Liang, Z. Chen, X. Chen, Y. Li, *J. Mater. Chem. A* **2019**, *7*, 20310.
[10] H. Zhang, M. Zhao, H. Liu, S. Shi, Z. Wang, B. Zhang, L. Song, J. Shang, Y. Yang, C. Ma, L. Zheng, Y. Han, W. Huang, *Nano Lett.* **2021**, *21*, 2255.
[11] T. Tan, P. Tao, X. Li, S. Imhanria, J. Deng, W. Wang, *Catal. Commun.* **2020**, *146*, 106135.
[12] T. Wang, Z. Kou, S. Mu, J. Liu, D. He, I. Amiinu, W. Meng, K. Zhou, Z. Luo, S. Chaemchuen, F. Verpoort, *Adv. Funct. Mater.* **2018**, *28*, 1705048.
[13] Q. Wang, Y. Lei, Z. Chen, N. Wu, Y. Wang, B. Wang, Y. Wang, *J. Mater. Chem. A* **2018**, *6*, 516.
[14] W. Niu, Z. Li, K. Marcus, L. Zhou, Y. Li, R. Ye, K. Liang, Y. Yang, *Adv. Energy Mater.* **2018**, *8*, 1701642.
[15] W. Xie, Y. Song, S. Li, J. Li, Y. Yang, W. Liu, M. Shao, M. Wei, *Adv. Funct. Mater.* **2019**, *29*, 1906477.
[16] Q. Hu, G. Li, X. Liu, B. Zhu, X. Chai, Q. Zhang, J. Liu, C. He, *Adv. Energy Mater.* **2019**, *9*, 1803867.
[17] X. Shu, S. Chen, S. Chen, W. Pan, J. Zhang, *Carbon* **2020**, *157*, 234.
[18] R. Zhao, J. Chen, Z. Chen, X. Jiang, G. Fu, Y. Tang, W. Jin, J. Lee, S. Huang, *ACS Appl. Energy Mater.* **2020**, *3*, 4539.
[19] C. Li, Z. Yu, H. Liu, M. Xiong, *Chem. Eng. J.* **2019**, *371*, 433.
[20] Y. Li, K. Zang, X. Duan, J. Luo, D. Chen, *J. Energy Chem.* **2021**, *55*, 572.
[21] X. Lv, Z. Xiao, H. Wang, X. Wang, L. Shan, F. Wang, C. Wei, X. Tang, Y. Chen, *J. Energy Chem.* **2021**, *54*, 626.
[22] S. Zhou, F. Dai, C. Dang, M. Wang, D. Liu, F. Lu, H. Qi, *Green Chem.* **2019**, *21*, 4732.
[23] J. Zhang, M. Zhang, Y. Zeng, J. Chen, L. Qiu, H. Zhou, C. Sun, Y. Yu, C. Zhu, Z. Zhu, *Small* **2019**, *15*, 1900307.
[24] J. Luo, H. Zhang, X. Qi, J. Yu, Z. Zhang, J. Wei, Z. Yang, *Carbon* **2020**, *162*, 36.
[25] D. Chen, J. Zhu, X. Mu, R. Cheng, W. Li, S. Liu, Z. Pu, C. Lin, S. Mu, *Appl. Catal., B* **2020**, *268*, 118729.
[26] Y. Wang, J. Hao, J. Yu, H. Yu, K. Wang, X. Yang, J. Li, W. Li, *J. Energy Chem.* **2020**, *45*, 119.
[27] B. Jinga, S. Youb, Y. Ma, Z. Xing, H. Chen, Y. Dai, C. Zhang, N. Ren, J. Zou, *Appl. Catal., B* **2019**, *244*, 465.
[28] X. Peng, L. Zhang, Z. Chen, L. Zhong, D. Zhao, X. Chi, X. Zhao, L. Li, X. Lu, K. Leng, C. Liu, W. Liu, W. Tang, K. Loh, *Adv. Mater.* **2019**, *31*, 1900341.
[29] Y. Wang, M. Yang, S. Liu, W. Shen, R. He, Y. Jiang, M. Li, *Energy Technol.* **2019**, *7*, 1900610.
[30] Y. Zheng, H. Song, S. Chen, X. Yu, J. Zhu, J. Xu, K. Zhang, C. Zhang, T. Liu, *Small* **2020**, *16*, 2004342.
[31] Z. Huang, J. Wang, Y. Peng, C. Jung, A. Fisher, X. Wang, *Adv. Energy Mater.* **2017**, *7*, 1700544.
[32] Q. Wang, X. Lu, Y. Tong, G. Li, *Adv. Sci.* **2018**, *5*, 1700515.
[33] L. He, F. Weniger, H. Neumann, M. Beller, *Agnew. Chem., Int. Ed.* **2016**, *55*, 12582.
[34] X. Xu, S. You, L. Yang, Z. Xing, S. Pan, Z. Cai, Y. Dai, J. Zou, *Biosens. Bioelectron.* **2018**, *102*, 101.
[35] Y. Lv, Y. Lin, L. Yang, Z. Cai, B. Jing, J. Yuc, X. Jiang, Z. Xing, J. Zou, *Chem. Eng. J.* **2018**, *342*, 228.
[36] C. Dang, Z. Huang, Y. Chen, S. Zhou, X. Feng, G. Chen, F. Dai, H. Qi, *ACS Appl. Mater. Interfaces* **2020**, *12*, 21528.
[37] C. Hu, H. Jin, B. Liu, L. Liang, Z. Wang, D. Chen, D. He, S. Mu, *Nano Energy* **2021**, *82*, 105714.
[38] S. Zhou, H. Qi, *Nanoscale* **2020**, *12*, 17373.
[39] H. Chen, T. Liu, J. Mou, W. Zhang, M. Liu, *Nano Energy* **2019**, *63*, 103836.
[40] N. Torad, R. Salunkhe, Y. Li, H. Hamoudi, M. Imura, Y. Sakka, C. Hu, Y. Yamauchi, *Chem. - Eur. J.* **2014**, *20*, 7895.
[41] Q. Xu, H. Jiang, Y. Li, D. Liang, Y. Hu, C. Li, *Appl. Catal., B* **2019**, *256*, 117893.
[42] H. Zou, G. Li, L. Duan, Z. Kou, J. Wang, *Appl. Catal., B* **2019**, *259*, 118100.
[43] W. Peng, Y. Wang, X. Yang, L. Mao, J. Jin, S. Yang, K. Fu, G. Li, *Appl. Catal., B* **2020**, *268*, 118437.
[44] D. Guo, R. Shibuya, C. Akiba, S. Saji, T. Kondo, J. Nakamura, *Science* **2016**, *351*, 361.
[45] D. Xie, D. Yu, Y. Hao, S. Han, G. Li, X. Wu, F. Hu, L. Li, H. Chen, Y. Liao, S. Peng, *Small* **2021**, *17*, 2007239.
[46] G. Kresse, D. Joubert, *Phys. Rev. B* **1999**, *59*, 1758.
[47] W. Kohn, L. Sham, *Phys. Rev.* **1965**, *140*, A1133.
[48] P. Hohenberg, W. Kohn, *Phys. Rev.* **1964**, *136*, B864.
[49] J. Perdew, K. Burke, M. Ernzerh, *Phys. Rev. Lett.* **1996**, *77*, 3865.
[50] H. Monkhorst, J. Pack, *Phys. Rev. B* **1976**, *13*, 5188.
[51] Z. Xue, X. Zhang, J. Qin, R. Liu, *J. Mater. Chem. A* **2019**, *7*, 23091.
[52] X. Wang, J. Liu, Z. Liu, W. Wang, J. Luo, X. Han, X. Du, S. Qiao, J. Yang, *Adv. Mater.* **2018**, *30*, 1800005.
[53] H. Jiang, J. Gu, X. Zheng, M. Liu, X. Qiu, L. Wang, W. Li, Z. Chen, X. Ji, J. Li, *Energy Environ. Sci.* **2019**, *12*, 322.

 

[54] S. S. Wu, Y. G. Zhu, Y. F. Huo, Y. C. Luo, L. H. Zhang, Y. Wan, B. Nan, L. J. Cao, Z. Y. Wang, M. C. Li, M. Y. Yang, H. Cheng, Z. G. Lu, *Sci. China: Mater.* **2017**, *60*, 654.
[55] R. Hao, J. J. Chen, Z. Y. Wang, J. J. Zhang, Q. M. Gan, Y. F. Wang, Y. Z. Li, W. Luo, Z. Q. Wang, H. M. Yuan, C. L. Yan, W. Zheng, Y. P. Huang, P. G. Liu, J. Yan, K. Y. Liu, C. Liu, Z. G. Lu, *Sci. China Mater.* **2021**, 64, 2987.
[56] R. Hao, S. Gu, J. J. Chen, Z. Y. Wang, Q. M. Gan, Z. Q. Wang, Y. P. Huang, P. G. Liu, K. L. Zhang, K. Y. Liu*, C. Liu*, Z. G. Lu, *Mater. Today Energy* **2021**, *21*, 100826.
[57] M. Reda, H. Hansen, T. Vegge, *Catal. Today* **2018**, *312*, 118.
[58] G. Zhu, F. Liu, Y. Wang, Z. Wei, W. Wang, *Phys. Chem. Chem. Phys.* **2019**, *21*, 12826.